

Experimental study on a pilot-scale medium-temperature latent heat storage system with various fins

Laiquan Lv^a, Yang Zou^b, Shengyao Huang^a, Xinyi Wang^b, Rongyu Shao^a, Xue Xue^a, Yan Rong^a, Hao Zhou^{a,*}

^a State Key Laboratory of Clean Energy Utilization, Institute for Thermal Power Engineering, Zhejiang University, Hangzhou, 310027, PR China

^b Shanghai Boiler Works Co., Ltd., Shanghai, 200000, PR China

ARTICLE INFO

Keywords:

Phase change material
Heat exchanger
Fin-and-tube
Medium-high temperature
Thermal energy storage

ABSTRACT

In this article, a pilot-scale latent heat storage system loaded with 5674.7 kg medium-temperature phase change material (PCM), having four groups of tubes embedded with various fins (longitudinal, H-shaped, spiral, and without fins), was designed and built. During the charging process, the smooth tube had the highest outlet temperature, followed by the tubes with longitudinal, H-shaped, and spiral fins, indicating that the spiral fins had the best heat transfer performance while the smooth's was the worst. The temperature difference in the vertical direction of the thermal energy storage unit was more significant than that in the horizontal direction. Besides, the thermal insulation performance test indicated that the temperature of PCM in the upper part decreased more slowly than that in the lower part due to the charging of the latent heat system being conducted from top to down. Moreover, after charging for 6.5 h, the accumulative energy and the mean power of the tubes with longitudinal, H-shaped, spiral, and without fins were 500.67, 541.57, 567.35, 432.56 MJ, 21.39, 23.14, 24.24, and 18.48 kW, respectively. The calculated charging efficiency of the latent heat storage system was 66.48%.

1. Introduction

Solar energy has become the most attractive renewable energy due to its ample supply, easy access, and environmental friendliness [1,2]. However, solar energy distributes unevenly, no matter in time or space. Thermal energy storage (TES) is crucial to address the mismatch between intermittent solar energy supply and demand [3,4].

Essentially, TES methods can be divided into sensible heat storage, latent heat storage, and thermochemical storage [5]. Latent heat storage (LHS) employs PCMs for TES that exhibit relatively high energy density and approximately constant temperature during phase transition [6,7]. Nevertheless, the low thermal conductivity of PCMs leads to poor heat charging and discharging rate, seriously affecting their development and application.

There are mainly two solutions to the poor heat charging and discharging rate of the LHS system, including enhancing the thermal conductivity of PCMs and improving the heat exchange performance of the LHS system [8]. The thermal conductivity of PCMs can be enhanced by additives in different dimensions, including 0D additives, for instance, metal [9] and metal oxide nanoparticles [10], 1D additives, such as

metal nanowires [11], carbon fiber [12] and carbon nanotube [13], 2D additives, for example, boron nitride [14], graphene [15], and graphene oxide [16], 3D additives, such as 3D carbon materials [17], metal-organic frameworks and their derivatives. Among them, 0D additives with inherently high thermal conductivity can build a conductive network, while 1D additives apply their structure and high thermal conductivity to establish linear conductive channels. Besides, 2D additives take advantage of large specific surface area to create surface thermal conductivity transmission, while 3D additives have their intrinsic 3D-conductive networks. Detailed explanations and specific contents can be found in Refs. [18,19].

Several approaches have been proposed to improve the heat exchange performance of the LHS system, including employing fins, geometric modification [20,21], and using multiple PCM arrangements [22, 23]. Employing fins is the most common approach to improve the heat exchange performance of the LHS system. Various operating conditions and design parameters need to be considered in designing a PCM-based shell and tube type, triple concentric tube type heat exchangers, along with the various heat transfer techniques, were reviewed by Kalapala and Devanuri [24]. Hu et al. [25] described the progress of close-contact melting research, including basic mechanisms, applications, and

* Corresponding author.

E-mail address: zhouhao@zju.edu.cn (H. Zhou).

<https://doi.org/10.1016/j.renene.2023.01.089>

Received 2 October 2022; Received in revised form 11 January 2023; Accepted 24 January 2023

Available online 25 January 2023

0960-1481/© 2023 Elsevier Ltd. All rights reserved.

Nomenclature		P	power (kW)
<i>Abbreviation</i>		T	temperature (°C)
DSC	differential scanning calorimetry	<i>Greek letter</i>	
DTG	derivative thermogravimetry	ΔH	latent heat (kJ/kg)
HTF	heat transfer fluid	η	efficiency
LHS	latent heat storage	μ	dynamic viscosity (mPa·s)
PCM	phase change material	ρ	density (kg/m ³)
TES	thermal energy storage	<i>Subscripts</i>	
TG	thermogravimetry	after	after the charging process
XRD	X-ray diffraction	before	before the charging process
<i>Symbol</i>		in	the HTF inflow of the heat exchange tube
c_p	specific heat (kJ/kg·K)	l	liquid
E	accumulative energy (kJ)	m	melting
k	thermal conductivity (W/(m·K))	out	the HTF outflow of the heat exchange tube
m	mass (kg)	s	solid

enhancement methods. Also, existing theoretical models, experimental observations, and numerical methods were systematically reviewed. Besides, Sciacovelli et al. [26] proposed to enhance the shell and tube LHS system performance by using tree-shaped fins and optimizing the geometry of Y-shaped primary and bifurcated wings by combining CFD simulation and response surface methodology. The results showed that the optimized unit could increase the system efficiency by 24%. Duan et al. [20] conducted a numerical study on the enhancement efficiency of the novel multi-spiral fins compared with the longitudinal fin. They also discussed PCM's melting and solidification rate in the annulus with 4, 8, and 16 spiral fins and three kinds of distortion degrees of fins. The numerical results showed that when the number of fins was fixed, the total melting and solidification time of PCM in the annulus with spiral fins were 57.60% and 74.13% less than those of longitudinal fins, respectively. When the distortion degree was the same, the melting and solidification time of 8 and 16 fins could be saved by 60.88% and 73.49% compared to 4 fins. Liu et al. [21] put forward an innovative longitudinal triangular fin structure, compared it with the conventional rectangular fin in terms of solidification behavior, and studied the effects of fin geometric parameters, initial temperature, and fin material on solidification performance. The results showed that the proposed longitudinal triangular fin could significantly improve the solidification performance, and the solidification time of PCM was shortened by 38.30% compared with the conventional rectangular fin. More information about improving the performance of the LHS system by employing fins can be found in Refs. [24,27].

Since the experimental studies of LHS systems are essential to the development of LHS systems, the experimental researches on lab-scale, small-scale, and pilot-scale LHS systems are reviewed. Lin et al. [28] investigated the TES performance and phase change behavior of sebacic/expanded graphite composite in a lab-scale double helix coil heat exchanger. The experimental results indicated that the temperature distribution in the LHS system was uniform. Increasing the heat transfer fluid (HTF) flow rate had a small impact on reducing charging time, while a 40 °C increase in inlet temperature could reduce charging time by 60%. Wu et al. [29] investigated the feasibility of an expanded-graphite/paraffin PCM-based heat exchanger operating as an instant air source water heater and compared the difference between the PCM-based water heater and traditional water tank. The authors confirmed that applying the PCM-based water heater could significantly reduce the traditional water tank volume.

Besides, several experimental studies on the charging/discharging performance of small-scale LHS systems were conducted by some scholars. A pillow plate heat exchanger with multiple flow channels was introduced by Lin et al. [30], and the PCM and HTF were sodium acetate

trihydrate and water, respectively. The heat exchanger's outlet water temperature, thermal power, heat energy efficiency, and heat transfer coefficient were evaluated. The experimental results showed that the energy released by the system could reach 6.3 MJ and the average power was 4 kW. Medrano et al. [31] experimentally studied the heat transfer performance of five small heat exchangers used as LHS systems during melting and solidification. Commercial RT35 was deployed as PCM, and water was used as HTF. It was found that the performance of the double tube heat exchanger with PCM embedded in graphite matrix was the best.

Furthermore, Besagni and Croci [32] developed a pilot-scale LHS system whose size was selected to be combined with a solar-assisted heat pump. Commercial paraffin RT26 and water were applied as PCM and HTF. The LHS system operation considered two heat exchanger configurations (parallel and series configurations) and implemented a wide set of boundary conditions to test the unit under relevant operating conditions. The study found that the proposed storage could store 65% more thermal energy than water storage with an equivalent volume. Gil et al. [33] confirmed that the cooling rate of the d-mannitol was a vital parameter in the formation of the different polymorphic phases based on a pilot-scale storage tank, which was consistent with the DSC result. Also, Peiró et al. [34] took advantage of the multiple PCMs configuration based on a pilot plant TES system for experimental evaluation. Three configurations were assessed: (1) single PCM with hydroquinone, (2) single PCM with d-mannitol, and (3) multiple PCM with hydroquinone and d-mannitol. The result indicated that the multiple PCMs configuration introduced an effectiveness enhancement of 19.36% compared with single PCM configuration as well as a higher uniformity on the HTF temperature difference between the inlet and outlet.

The current researches mainly focus on the experimental and numerical investigation of employing different innovative fins to improve the performance of LHS systems, along with the experimental study of small-scale and low-temperature novel heat exchangers. Due to the broader application and stronger attraction of medium-high temperature TES (such as waste heat recovery and generation of medium-temperature steam), a pilot-scale LHS system with four groups of tubes embedded with various fins (longitudinal, H-shaped, spiral, and without fins) was designed and built. The system could collect medium-high temperature thermal energy (200–295 °C) and has relatively stable power input during the charging process. Besides, the effects of various heat exchange fins on the charging process were experimentally investigated, and some valuable parameters for practical applications, including temperature difference in various directions, thermal insulation, and energy storage performance, were provided.

2. Experimental system and procedure

2.1. Experimental system

A pilot-scale LHS system was designed to investigate and compare the effects of various heat exchange fins (longitudinal, H-shaped, and spiral fins) on the charging process and obtain critical technical parameters. The experimental system mainly consists of a pilot-scale TES unit, a heat transfer oil circulating heating section, and a data acquisition unit, as depicted in Fig. 1.

2.1.1. Pilot-scale TES unit

As exhibited in Fig. 1 (a), the main part of the TES unit is a cubic horizontal shell-and-tube TES device in which high-temperature heat transfer oil flows on the tube side to heat the PCM filled on the shell side. The top and bottom of the device have a filler and a discharge port for loading and unloading PCM. Besides, there is a vent port at the top of the device to prevent air expansion from causing excessive pressure on the shell side. After the installation of the TES unit and the connection of pipes were completed, the surface was covered with silicon insulation foam with a thickness of approximately 20 mm (Fig. 1 (b)).

The TES unit contains four groups of heat exchange tubes, i.e., employed with longitudinal, H-shaped, spiral, and without fins from left to right. These groups of tubes are the same except for the fins embedded

in the tube wall shell. Each group of tubes has 17 layers with 4 heat exchange tubes per layer, for a total of 68 tubes per group. The turning of the tubes in the TES unit is done by the same type of vertical and horizontal U-tubes. The tubes are made of carbon steel, with an outer and inner diameter of 38 and 32 mm, respectively, and the spacings of horizontal and vertical tubes are 92 mm. The detailed dimensions of the pilot TES unit and the locations of the thermocouples are represented in Fig. 2. Fig. 3 and Table 1 summarize the parameters of various fins embedded in the heat exchange tubes, which were designed according to the same volume of fins on the shell side.

2.1.2. Heat transfer oil circulating heating section

The fundamental function of the section is to provide high-temperature heat transfer oil for the TES unit to realize the charging of PCM. This section consists of a heat transfer oil circulating boiler (YDW-225, maximum operating temperature of 300 °C and maximum power of 225 kW), inlet header, outlet header, branches, valves, and flowmeters (LUGB-15C, flow range of 0–80 L/min and a measuring error of $\pm 1.5\%$). The heat transfer oil boiler is responsible for heating the heat transfer oil and controlling the output temperature of the oil. The heat transfer oil is heated to a specified temperature and then flows from above to four groups of tube bundles, through the inlet header of the TES unit and out of the tubes below. Since the upper PCM in the TES device is in direct contact with the high-temperature heat transfer oil, the PCM

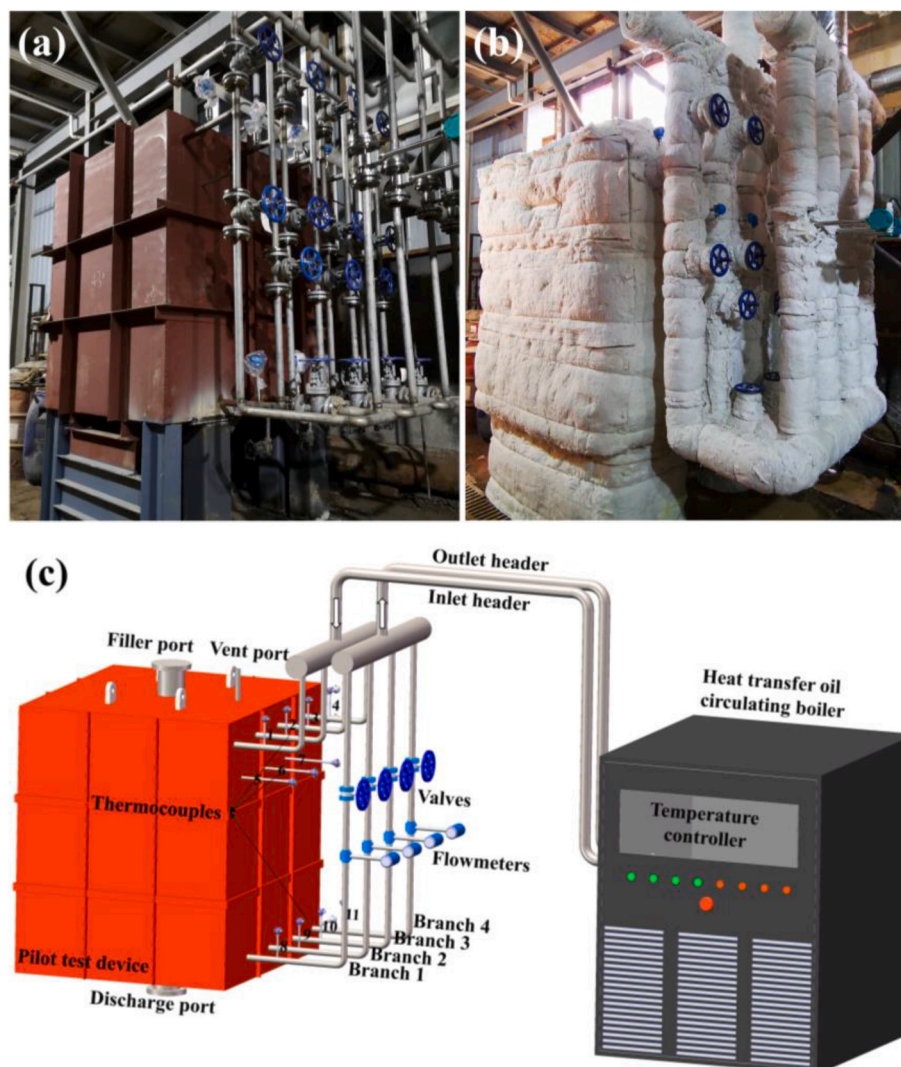


Fig. 1. Photographs of the pilot-scale TES unit (a) before and (b) after covering with insulation, and (c) schematic diagram of the experimental LHS system for TES.

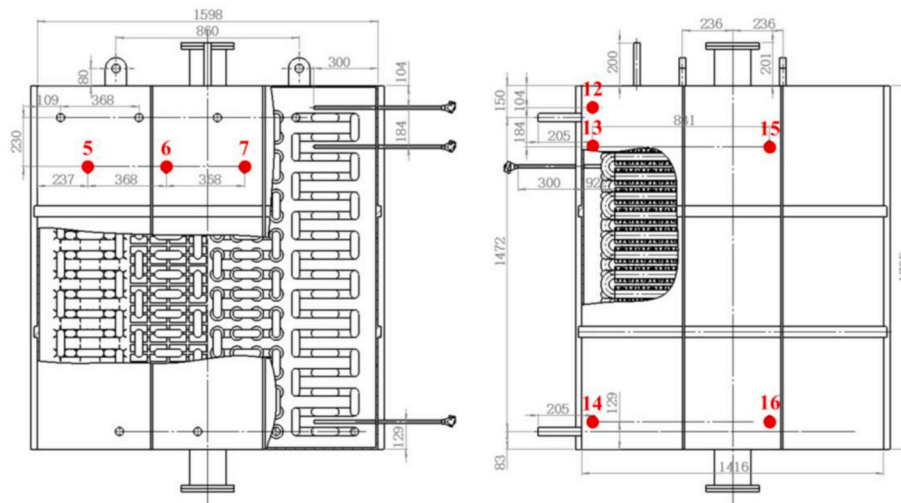


Fig. 2. Details dimensions of the pilot TES unit and thermocouples locations (unit: mm).

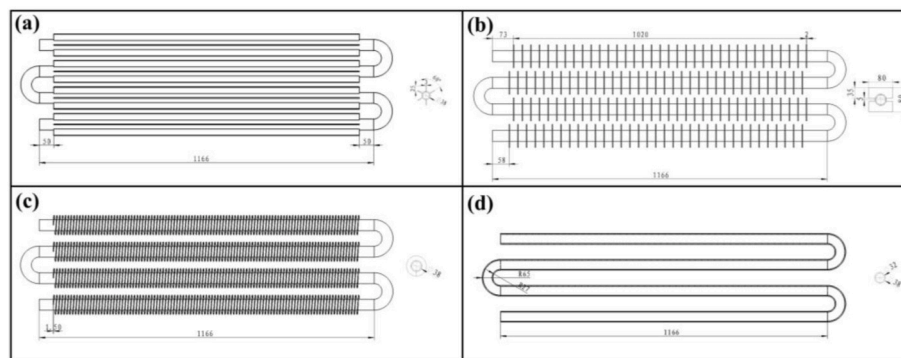


Fig. 3. Details of various fins embedded in the heat exchange tubes (unit: mm).

Table 1
Parameters of various fins embedded in the heat exchange tubes.

Fin type	Parameters
Longitudinal	Angle: 60°, number: 6, height: 25 mm, and thickness: 3 mm
H-shaped	Spacing: 28 mm, length: 80 mm, width: 35 mm × 2, and thickness: 2 mm
Spiral	Pitch: 10 mm, height: 15 mm, and thickness: 1.5 mm

will melt first, which provides some room for the expansion of liquid PCM whose density is less than solid PCM, preventing considerable thermal stress on the TES device. The cooled heat transfer oil flows back to the boiler to continue heating, forming a cycle.

2.1.3. Data acquisition section

A total of 16 thermocouples (K-type, temperature measurement range: 0–1100 °C and measurement error: ±1 °C) were installed in the LHS system to monitor the temperatures of PCM and heat transfer oil. Among them, eight thermocouples were installed at the inlet (#1, #2, #3 and #4) and outlet (#8, #9, #10 and #11) of the heat exchange tubes to represent the inlet and outlet temperatures of heat transfer oil, as exhibited in Fig. 1. Moreover, another eight thermocouples were installed on the shell side of the TES unit to monitor the temperature of PCM. The thermocouples #5, #6, and #7 monitor the temperatures of the PCM near the heat exchanger tubes with longitudinal, H-shaped and spiral fins, while the temperature of the PCM near smooth heat exchanger tube is represented by thermocouple #13. The values of thermocouples #12, #13, #15 and, #14, #16 represent the

temperatures of upper and lower PCM in the TES unit, respectively. The specific thermocouple location arrangement is displayed in Fig. 2.

2.2. Thermophysical properties of PCM, carbon steel, and heat transfer oil

The stability and reliability of medium-temperature PCMs are crucial for the operation of the LHS system. Based on these requirements, a commercial medium-temperature PCM was purchased from HeatMate Technology (Shanghai) Co., Ltd. In addition to the density and viscosity provided by the manufacturer, other thermophysical properties of the PCM used in the study were obtained through experimental characterization. Besides, the tubes and fins in the pilot-scale TES units are carbon steel. The HTF is heat transfer oil (Therminol L-60), bought from Eastman Chemical Co., Ltd. Table 2 summarizes the thermophysical of PCM,

Table 2
Thermophysical properties of PCM, carbon steel, and heat transfer oil.

Properties	Symbol	Units	PCM	Carbon steel	Heat transfer oil (200 °C/ 290 °C)
Solidus/liquidus density	ρ_s/ρ_l	kg/m ³	2213.5/1924.6	7850	868/792
Specific heat	c_p	kJ/(kg·K)	–	0.47	2.209/2.520
Thermal conductivity	k	W/(m·K)	–	48.85	0.1079/0.096
Dynamic viscosity	μ	mPa·s	4.34	–	0.62/0.323

carbon steel, and heat transfer oil.

2.3. Characterization methods

A differential scanning calorimeter, DSC (DSC25, TA, USA, uncertainty: ± 0.05 °C for temperature, $\pm 0.1\%$ for phase change enthalpy, the scanning rate of 10 °C/min, constant N₂ stream of 50 mL/min) in dynamic mode obtained the PCM's melting temperature, solidification temperature, and latent heat at 100–300 °C as well as PCM's specific heat at 30–300 °C. A thermogravimetric analyzer (TGA 5500, TA, USA, accuracy: ± 0.1 °C, $\pm 0.01\%$, the heating rate of 10 °C/min, constant N₂ stream of 60 mL/min) characterized the thermal stability of PCM for the size of samples 6–7 mg with the temperature range of 30–600 °C. X-ray diffraction, XRD (X'pert Powder, PANalytical B.V., Netherland) with Cu K-alpha radiation ($k = 1.540598$ Å) characterized the crystal size of the samples under room temperature. The scanning range, scanning rate, and step size were 10°–80°, 0.1°/min, and 0.02°, respectively. The PCM's thermal conductivity was characterized by a thermal constant analyzer (TCi, C-Therm, Canada, accuracy: $\pm 1\%$) at a room temperature of 20 ± 0.5 °C. The PCM samples were melted at 300 °C and poured into a mold (diameter: 50 mm) for cooling to obtain PCM blocks. Both surfaces of the blocks were then carefully polished for the thermal conductivity test to avoid the experimental error caused by the samples as much as possible. The result significantly different from the average value obtained by the test would be eliminated. Finally, the mean value obtained from the test without abnormal results was applied as the thermal conductivity result.

2.4. Experimental procedure

After the installation of the pilot TES unit, the heat transfer oil circulating heating section, and the data acquisition section was completed, the loading of the PCM began. When the temperature of the output oil reached 300 °C, the oil started to circulate and flowed from top to bottom in the TES unit. Simultaneously, the PCM was poured into the TES unit through the filler port. PCM loading was completed until the liquid level of PCM was close to the filler port. After PCM loading was finished, the thermocouples continued to monitor the TES unit's temperature change to obtain the LHS system's thermal insulation performance.

The charging process is divided into seven stages, as listed in Table 3. When the temperature of the TES unit was below 200 °C, the pump and valve were opened, and the TES unit was preheated by circulating heat transfer oil until the temperature of the TES unit rose to 210 °C. The mean value of the measured thermocouples #15 and #16 was applied as the temperature of the TES unit. After the preheating process, the bypass valve was turned on, and the main valve was turned off, and the oil temperature would continue to rise without flowing through the TES unit. When the output temperature of the oil increased to 255 °C, closed the bypass valve and opened the main valve to continue the charging process.

When the PCM in the TES unit was solid (200–220 °C), the temperature of the oil output from the boiler would increase by 5 °C for every

Table 3
Operating parameters of the pilot TES unit at different charging stages.

Stage	The temperature of the TES unit (°C)	Oil flow in the main tube (L/h)	Oil flow in the branch tube (L/h)	Inlet temperature of the oil (°C)
1	<200	4000	1000	210
2	200–210	4000	1000	255
3	210–220	4000	1000	260
4	220–230	4000	1000	265
5	230–240	4000	1000	280
6	240–250	4000	1000	285
7	250–260	4000	1000	290

10 °C increase in the temperature of PCM. Further, as the PCM was in the solid-liquid phase (220–230 °C), the oil temperature would increase by 15 °C for every 10 °C increase in the temperature of PCM. Finally, when the PCM was in the liquid phase (230–260 °C), the oil temperature would increase by 5 °C for every 10 °C increase in the temperature of PCM. The charging process was completed as soon as the temperature of the TES unit was 270 °C.

2.5. Uncertainty analysis

The uncertainty in the study comes from the thermocouple and flowmeter readings. The manufacturers of thermocouples and flowmeters give these uncertainty values. The uncertainty in the temperature measurements recorded by thermocouples #1–16 is within 1% and will not be further discussed. However, the uncertainty of calculated energy storage performance parameters, including mean power, input energy, and charging efficiency, is significant and presented in the results and discussion section.

3. Results and discussion

3.1. Thermophysical properties of PCM

The DSC test reveals the melting temperature, solidification temperature, and latent heat of PCM (Fig. 4 (a)), i.e., 210.75, 262.58, 226.73 °C, and 128.15 kJ/kg for the onset, offset, peak temperature, and latent heat at endothermic and 252.14, 199.03, 249.29 °C, and 125.00 kJ/kg at exothermic, respectively. The TG and DTG curves show that the mass of PCM was almost unchanged before 500 °C and decreased significantly after the temperature exceeded 500 °C, indicating that the sample started to decompose (Fig. 4 (b)). The specific heat capacity of PCM exhibited two peaks at 30–300 °C, which may be caused by the melting of different components in the initial sample. After removing the phase change interval, the average specific heat capacity of PCM in the operating temperature interval, i.e., 200–290 °C, of the LHS system was 1.238 kJ/(kg·K) (Fig. 4 (c)).

Moreover, the XRD pattern of PCM is displayed in Fig. 4 (d). Several strong diffraction peaks located at 23.62°, 29.48°, 33.72°, 39.02°, 47.94°, 48.42°, and 55.64° were observed. The transient plane heat source method obtained the thermal conductivity of PCM was 0.503 \pm 0.002 W/(m·K).

3.2. Temperature analysis during the charging process

The TES unit was loaded with 5674.7 kg of PCM over 5 days until the liquid PCM completely submerged the heat exchanger tubes and fins. Fig. 5 (a) shows the HTF volume flow rate variation for each heat exchange tube during the charging process, where the mean values for the tubes with longitudinal, H-shaped, spiral, and without fins were 916.29, 905.79, 868.71, and 904.17 L/h, respectively.

The evolution of inlet temperatures (thermocouples #1, #2, #3, and #4) and outlet temperatures (thermocouples #8, #9, #10, and #11) over time during the charging process is dispatched in Fig. 5 (b). The inlet temperatures of the TES unit showed a step-wise rise, and the temperature rise program was determined by the internal temperature of the TES unit (the average temperature of thermocouples #15 and #16). After preheating for about 1 h, the inlet valves were closed temporarily so that the HTF could achieve internal circulation. When the temperature of HTF increased to 255 °C, the inlet valves of the TES unit were opened again.

As displayed in Fig. 5 (b), the smooth tube has the highest outlet temperature (#11), followed by the tubes with longitudinal fins (#8), H-shaped fins (#9), and spiral fins (#10), which indicates that the spiral fins has the best heat transfer performance, while the smooth is the worst.

Due to the regulating effect of the HTF temperature control system,

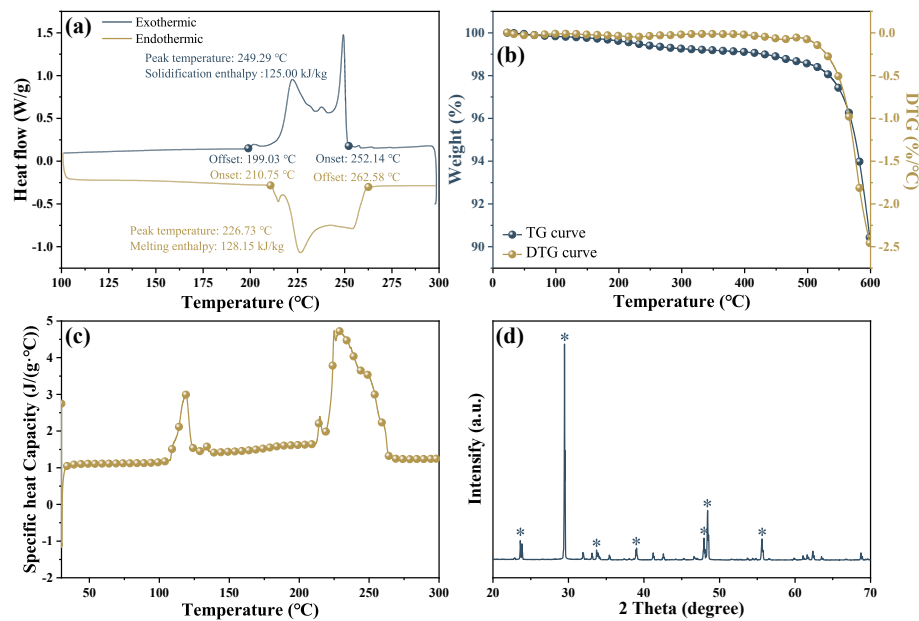


Fig. 4. Thermophysical properties of the deployed PCM: (a) DSC, (b) TG and DTG, (c) specific heat capacity, and (d) XRD curves.

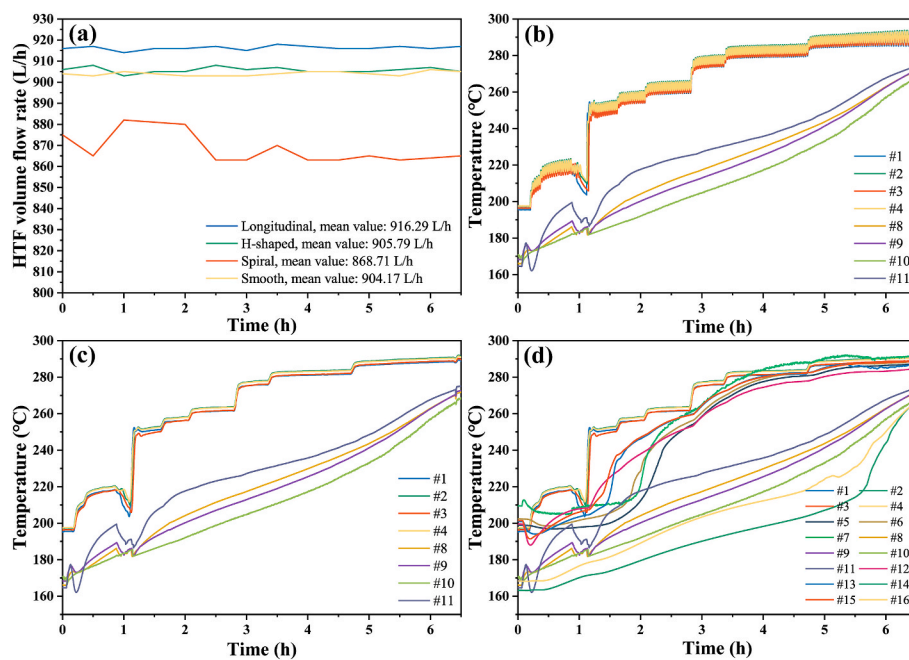


Fig. 5. Evolution of (a) HTF volume flow rate, (b) inlet (thermocouples #1, #2, #3 and #4) and outlet temperatures (thermocouples #8, #9, #10 and #11), (c) inlet and outlet temperatures after smooth, (d) all temperatures monitored by thermocouples over time for the charging process.

the inlet temperature of the HTF fluctuates greatly. The temperature profile of the inlet HTF was smoothed, and the processed temperature profile is shown in Fig. 5 (c). Fig. 5 (d) reveals the evolution of all temperatures monitored by thermocouples over time during the charging process.

Thermocouples #5–7, mounted on the front of the TES unit, exhibited the same temperature trend. They all increased slowly initially because the temperature difference between PCM and oil was small during the preheating process. After that, when the oil at 255 °C entered the TES unit, the temperature of thermocouples #5–7 increased quickly due to the heat conduction of solid PCM. Then their temperatures rose slowly again, indicating that the PCM near the thermocouples underwent a phase transition (Fig. 6 (a)). Subsequently, the temperature of

these thermocouples increased rapidly to a temperature close to the HTF entering the TES unit, indicating that the PCM around the thermocouples had completely melted. It is important to note that, among them, thermocouple #7 had the highest temperature, followed by #6 and #5, which further proved that the heat exchanger tube with spiral fins had the best heat transfer performance since thermocouple #7 was inserted between the tubes with spiral fins. Similarly, thermocouple #6 was inserted between the tubes with H-shaped fins and therefore had a higher temperature than thermocouple #5 inserted between the tubes with the longitudinal fins.

Furthermore, thermocouples #12, #13, and #15 had the same temperature trend as #5–7, while their temperatures rose faster, which was caused by the difference in their mounting heights, as plotted in

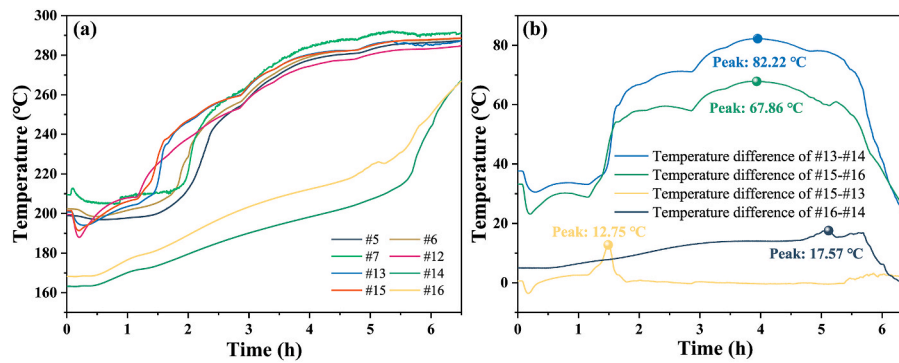


Fig. 6. Evolution of (a) the temperature of PCM (thermocouples #5–7 and #12–16) and (b) the temperature difference in the vertical (#13–#14 and #15–#16) and horizontal (#15–#13 and #16–#14) directions over time for the charging process.

Fig. 6 (a). The HTF entered from the top of the TES unit, exposing the PCM in the upper of the TES unit to the high-temperature HTF. The temperature of the HTF would drop significantly as the heat of HTF was transferred to the PCM, allowing the PCM in the upper to melt faster and increase in temperature more quickly. Similarly, thermocouples #14 and #16, located further down, increased rapidly in temperature only after about 5.5 h of charging, which was about 4 h later than about 1.5 h of thermocouples #12, #13 and #15. This indicated a large temperature difference between the upper and lower parts of the TES unit during the charging process. The PCM in the upper part melted before the PCM in the lower part, which may cause significant thermal stress in the TES unit. After approximately 5.5 h of charging, the temperature of thermocouples #14 and #16 gradually approached the outlet temperature of the TES unit, illustrating the end of the charging process.

To further illustrate the internal temperature distribution of the TES unit, the temperature difference in the vertical (#13–#14 and #15–#16) and horizontal (#15–#13 and #16–#14) directions was calculated (Fig. 6 (b)). The temperature difference of TES units in the horizontal direction was much smaller than that in the vertical direction, caused by the temperature difference of HTF.

For the vertical direction of the TES unit, the temperature difference of thermocouples #13–#14 and #15–#16 was small during the preheating process, with a temperature difference of about 25–35 °C. After that, the temperature difference increased rapidly, reaching maximum values of 88.22 and 67.86 °C at 3.95 and 3.92 h, respectively. As the charging proceeded, their values gradually decreased to approximately 20 °C. The reason for such a phenomenon was that the heat of the oil was used to increase the sensible heat of the solid PCM by heat conduction during the preheating process. The small inlet and outlet temperature difference of heat transfer oil led to a small temperature difference of PCM in the vertical direction during the preheating process. When the PCM in the upper part of the TES unit near the heat exchanger tube was completely melted, its temperature rapidly increased to a temperature close to the HTF, which led to a rapid increase in the temperature of #13 and #15 at higher positions. In comparison, the PCM in the lower part of the TES unit near the thermocouple was still melting because the HTF flowing through it was cooler, resulting in a lower PCM temperature. As a result, the temperature difference in the vertical direction of the TES unit gradually increased. As the liquid PCM increased, the natural convection of the liquid PCM gradually increased, which led to an increase in the melting rate and temperature of the lower PCM in the TES unit. Consequently, PCM's temperature rose rapidly to a temperature close to the HTF, and the temperature difference of #13–#14 and #15–#16 decreased rapidly. However, the temperature of the HTF at the lower location was still lower than that of the higher location, so there was still a temperature difference between the thermocouples.

For the temperature distribution of the TES unit in the horizontal direction, the temperature difference of #15–#13 reached the maximum value (12.748 °C at 1.49 h) earlier than that of #16–#14 (17.567 °C at

5.12 h), caused by the difference in the time of complete melting of the PCM near the heat exchanger tube at different heights. The higher positioned thermocouples #15 and #13 contacted a higher temperature HTF; thus, the PCM melted more quickly under heat conduction.

3.3. Thermal insulation performance

Fig. 7 plots the temperature curves of 16 thermocouples over time for the thermal insulation process. The temperature of the inlet (thermocouples #1, #2, #3, and #4) and outlet (thermocouples #8, #9, #10, and #11) first decreased rapidly, caused by the heat dissipation of HTF. Subsequently, they began to rise over time, probably due to the heating of the PCM with higher temperature. For the higher positioned thermocouples, whose temperatures decreased slightly, e.g., #6 and #15 dropped from 295.17 to 294.97 °C before to 261.49 and 261.17 °C after the insulation process. However, a significant temperature drop for the lower positioned thermocouples was observed during the thermal insulation process. The temperature of thermocouples #14 and #16 dropped from 293.81 to 293.72 °C to 210.54 and 213.52 °C. At the same time, the PCM near the lower positioned thermocouples solidified, which can be confirmed by the relatively flat temperature change during 15–20 h. The reason for this phenomenon could be that the temperature of the lower part of the TES unit was lower after charging, causing the PCM in the lower part to solidify first.

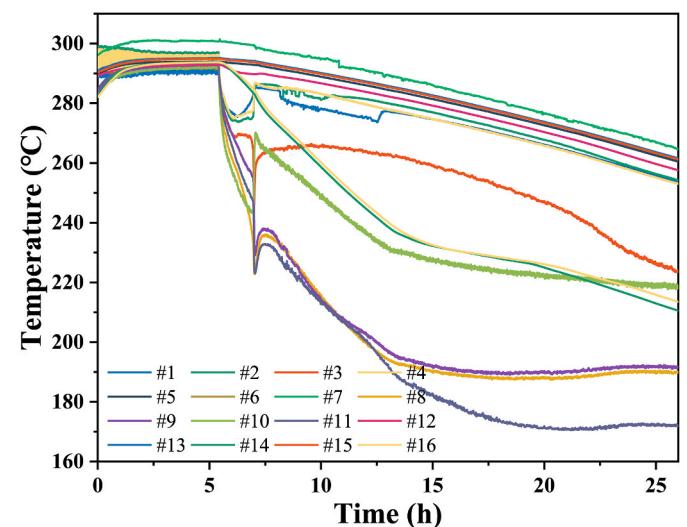


Fig. 7. Evolution of the temperature over time for the thermal insulation process.

3.4. Energy storage performance

Energy analysis, including power and accumulative energy, is essential to evaluate the performance of the LHS system and the heat transfer performance of various fins. By neglecting the heat loss of the LHS system, the instantaneous power of varying heat exchange tubes could be calculated by considering the temperature difference of the HTF, as the following equation (1) shows:

$$P = \dot{m}c_{p,HTF}(T_{in} - T_{out}) \tag{1}$$

where \dot{m} and $c_{p,HTF}$ are the mass flow rate and specific heat of HTF, and T_{out} and T_{in} are the temperatures of the HTF outflow and inflow of the heat exchange tubes. The accumulative energy of each heat exchange tube could be determined by multiplying power and time, as given in equation (2):

$$E = \int_0^t P \cdot dt \tag{2}$$

The evolution of accumulative energy and charging power of tubes with different fins with time during the charging process are plotted in Fig. 8 (a, b) and summarized in Table 4. The accumulative energy of the tubes with various fins was almost the same during the preheating process. Still, after increasing the temperature of the HTF to 255 °C, there are significant differences between these tubes. This is because the temperature difference between PCM and HTF was small during the preheating process, resulting in the low charging power of various tubes. As the HTF temperature raised, the charging power of these tubes increased rapidly. Different heat transfer performances led to accumulation energy variation, which could be further demonstrated by Fig. 8 (b). After 6.5 h of charging, the accumulative energy of the tubes with longitudinal, H-shaped and spiral fins was 500.67 ± 13.15, 541.57 ± 12.05, and 567.35 ± 11.03 MJ, respectively, which were 1.16, 1.25 and 1.31 times that of the smooth tube.

Based on the difference between the inlet and outlet temperatures of the HTF, the instantaneous power of tubes with different fins could be determined, as shown in Fig. 8 (b). During the preheating process, significant power fluctuations were observed in the tubes with various fins,

Table 4

Accumulative energy, mean power, and time of power greater than 20 kW of heat exchanger tubes with longitudinal, H-shaped, spiral, and without fins.

Heat exchanger tube	Accumulative energy (MJ)	Mean power (kW)	Time of power greater than 20 kW (h)
Longitudinal	500.67 ± 11.03	21.39 ± 1.70	4.00
H-shaped	541.57 ± 12.05	23.14 ± 1.85	4.22
Spiral	567.35 ± 13.15	24.24 ± 2.02	4.38
Smooth	432.56 ± 9.69	18.48 ± 1.49	2.86

which may be caused by the variation of the inlet temperature and the uneven temperature of HTF remaining in the TES unit. Subsequently, as long as the temperature of the HTF entering the TES unit was raised, the power of the tubes increased to varying degrees, depending on the amplitude of the raised temperature. As the heat of HTF was transferred to the PCM, the temperature difference between HTF and PCM gradually decreased, resulting in a decrease in instantaneous power. The mean power of tubes with longitudinal, H-shaped, and spiral fins was 21.39 ± 1.70, 23.14 ± 1.85, and 24.24 ± 2.02 kW, respectively, 1.16, 1.25 and 1.31 times that of the smooth tube. Besides, large instantaneous power fluctuations are not expected in the practical application of the LHS system, affecting the stable input and output of thermal energy. Therefore, a step-wise temperature raise approach was adopted to stabilize the power input during charging. It is evident from Fig. 8 (b) that the approach could effectively stabilize the power input during the charging process. The charging power of the tubes could be stabilized between 20 and 35 kW, except for the early and late charging periods. The time of instantaneous power greater than 20 kW for the tubes with longitudinal, H-shaped, and spiral fins was 4.00, 4.22, and 4.38 h, respectively, which were 1.40, 1.48, and 1.53 times that of the smooth tube, as revealed in Fig. 8 (d).

Furthermore, Fig. 8 (c) shows the evolution of the power ratio for the tube with longitudinal, H-shaped and spiral fins with the smooth tube over time. The instantaneous power of the tube with three different fins

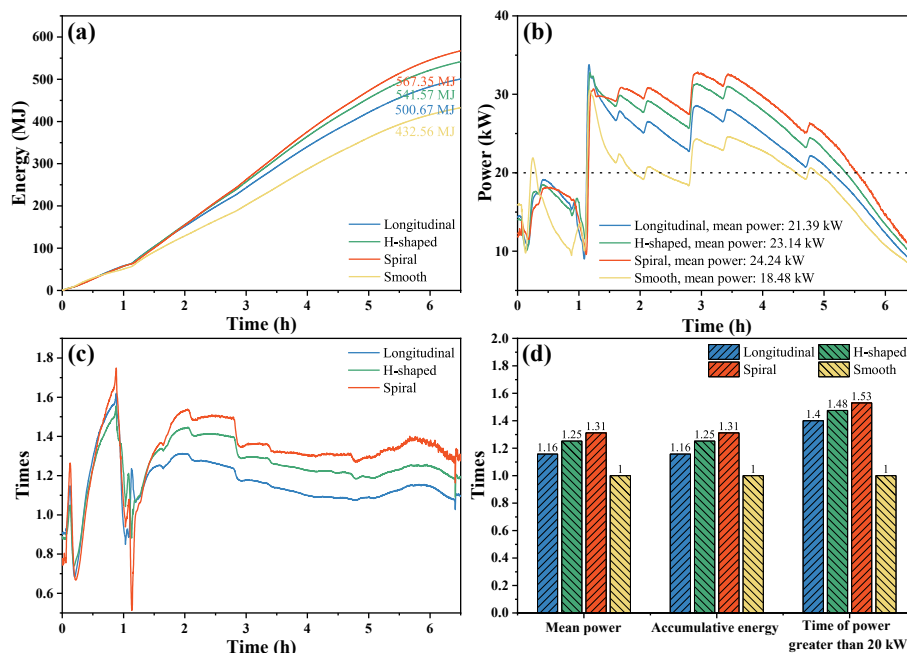


Fig. 8. Evolution of (a) accumulative energy and (b) instantaneous power of heat exchange tubes installed with various fins over time for charging process, (c) evolution of the ratio of the power for the tube installed longitudinal, H-shaped and spiral fins with the smooth tube over time, (d) the ratio of mean power, accumulative energy and time of power greater than 20 kW for the tube installed longitudinal, H-shaped and annual fins with the smooth tube.

was greater than that of the smooth tube for most of the charging process, providing further evidence that the best heat transfer performance was achieved by the tube with the spiral fins, followed by the H-shaped and longitudinal fins.

In addition, the charging efficiency of the LHS system during the charging process was calculated by equation (3):

$$\eta = \frac{Q_{\text{sensible}} + Q_{\text{latent}}}{E} = \frac{m_{\text{PCM}} \bar{c}_{p,\text{PCM}} (T_{\text{after}} - T_{\text{before}}) + m_{\text{PCM}} \Delta H_m}{E} \quad (3)$$

where Q_{sensible} , Q_{latent} , T_{after} , and T_{before} are the sensible, latent heat stored in the TES unit during charging and the temperature of the TES unit after and before charging, respectively. m_{PCM} , $c_{p,\text{PCM}}$, and ΔH_m are the mass of PCM loaded in the TES unit, the specific heat capacity and the melting enthalpy of PCM, respectively. The charging efficiency of the LHS system obtained according to equation (3) is $66.48 \pm 0.49\%$ because part of the heat from the HTF was lost or used to heat the other parts of the TES unit.

4. Conclusions

In this article, a pilot-scale LHS system loaded with 5674.7 kg PCM, having four groups of tubes embedded with various fins (longitudinal, H-shaped, spiral, and without fins), was designed and built. The LHS system can collect medium-temperature thermal energy and has a relatively stable power input. Thermophysical properties of the employed PCM were obtained by experimental characterization. The charging process of the LHS system was conducted to study the temperature change, thermal insulation performance, and energy storage performance. The primary conclusions of this article are as follows:

- (1) The melting, solidification temperature, latent heat, and thermal conductivity of employed PCM were 210.75, 252.4 °C, 128.5, 125.00 kJ/kg, and 0.503 W/(m·K). PCM's average specific heat capacity in the operating temperature interval was 1.238 kJ/(kg·K).
- (2) The smooth tube had the highest outlet temperature during the charging process, followed by the tubes with longitudinal, H-shaped, and spiral fins, indicating that the spiral fins had the best heat transfer performance, while the smooth was the worst. The temperature difference in the vertical direction (the maximum between #13 and #14 was 88.22 °C) of the TES unit was more significant than that in the horizontal direction (the maximum between #15 and #13 was 12.75 °C).
- (3) The temperature of the higher positioned thermocouples # 6 and #15 dropped from 295.17 and 294.97 °C to 261.49 and 261.17 °C after storage for 26 h, while that of the lower positioned thermocouples # 14 and #16 dropped from 293.81 and 293.71 °C to 210.54 and 213.52 °C, indicating the PCM near the lower positioned thermocouples solidified.
- (4) After charging for 6.5 h, the accumulative energy of the tubes with longitudinal, H-shaped, spiral, and without fins was 500.67, 541.57, 567.35, and 432.56 MJ, respectively. The mean power and the time of instantaneous input power greater than 20 kW of the tubes with longitudinal, H-shaped, spiral, and without fins were 21.39, 23.14, 24.24, 18.48 kW, 4.00, 4.22, 4.38, and 2.86 h, respectively.

CRedit authorship contribution statement

Laiquan Lv: Formal analysis, Investigation, Data curation, Writing – original draft, Project administration. **Yang Zou:** Funding acquisition. **Shengyao Huang:** Visualization, Investigation. **Xinyi Wang:** Funding acquisition. **Rongyu Shao:** Investigation. **Xue Xue:** Investigation. **Yan Rong:** Investigation. **Hao Zhou:** Conceptualization, Methodology, Validation.

Declaration of competing interest

The authors declare that they have no known competing financial interests or personal relationships that could have appeared to influence the work reported in this paper.

Acknowledgments

This study was supported by the Fundamental Research Funds for the Central Universities (2022ZFH004).

References

- [1] X. Yang, J. Guo, B. Yang, H. Cheng, P. Wei, Y.-L. He, Design of non-uniformly distributed annular fins for a shell-and-tube thermal energy storage unit, *Appl. Energy* 279 (2020), <https://doi.org/10.1016/j.apenergy.2020.115772>.
- [2] S. Sikiru, T.L. Oladosu, T.I. Amosa, S.Y. Kolawole, H. Soleimani, Recent advances and impact of phase change materials on solar energy: a comprehensive review, *J. Storage Mater.* 53 (2022), <https://doi.org/10.1016/j.est.2022.105200>.
- [3] M. Ibáñez, L.F. Cabeza, C. Solé, J. Roca, M. Nogués, Modelization of a water tank including a PCM module, *Appl. Therm. Eng.* 26 (11–12) (2006) 1328–1333, <https://doi.org/10.1016/j.applthermaleng.2005.10.022>.
- [4] D. Haillot, E. Franquet, S. Gibout, J.-P. Bédécarrats, Optimization of solar DHW system including PCM media, *Appl. Energy* 109 (2013) 470–475, <https://doi.org/10.1016/j.apenergy.2012.09.062>.
- [5] K. Hosseinzadeh, M.A.E. Moghaddam, A. Asadi, A.R. Mogharrebi, D.D. Ganji, Effect of internal fins along with Hybrid Nano-Particles on solid process in star shape triplex Latent Heat Thermal Energy Storage System by numerical simulation, *Renew. Energy* 154 (2020) 497–507, <https://doi.org/10.1016/j.renene.2020.03.054>.
- [6] K. Pielichowska, K. Pielichowski, Phase change materials for thermal energy storage, *Prog. Mater. Sci.* 65 (2014) 67–123, <https://doi.org/10.1016/j.pmatsci.2014.03.005>.
- [7] H. Nazir, M. Batool, F.J. Bolivar Osorio, M. Isaza-Ruiz, X. Xu, K. Vignarooban, P. Phelan, Inamuddin, A.M. Kannan, Recent developments in phase change materials for energy storage applications: a review, *Int. J. Heat Mass Tran.* 129 (2019) 491–523, <https://doi.org/10.1016/j.ijheatmasstransfer.2018.09.126>.
- [8] F. Agyenim, N. Hewitt, P. Eames, M. Smyth, A review of materials, heat transfer and phase change problem formulation for latent heat thermal energy storage systems (LHTES), *Renew. Sustain. Energy Rev.* 14 (2) (2010) 615–628, <https://doi.org/10.1016/j.rser.2009.10.015>.
- [9] W. Cui, Y. Yuan, L. Sun, X. Cao, X. Yang, Experimental studies on the supercooling and melting/freezing characteristics of nano-copper/sodium acetate trihydrate composite phase change materials, *Renew. Energy* 99 (2016) 1029–1037, <https://doi.org/10.1016/j.renene.2016.08.001>.
- [10] H. Zhou, L. Lv, M. Ji, Y. Zhang, F. Cheng, K. Cen, Experimental study of metal-oxide nanoparticles on the thermal properties of erythritol for thermal energy storage, *Asia-Pac. J. Chem. Eng.* 17 (2) (2022), <https://doi.org/10.1002/apj.2754>.
- [11] J.L. Zeng, Z. Cao, D.W. Yang, L.X. Sun, L. Zhang, Thermal conductivity enhancement of Ag nanowires on an organic phase change material, *J. Therm. Anal. Calorim.* 101 (1) (2009) 385–389, <https://doi.org/10.1007/s10973-009-0472-y>.
- [12] Q. Zhang, Z. Luo, Q. Guo, G. Wu, Preparation and thermal properties of short carbon fibers/erythritol phase change materials, *Energy Convers. Manag.* 136 (2017) 220–228, <https://doi.org/10.1016/j.enconman.2017.01.023>.
- [13] S. Shen, S. Tan, S. Wu, C. Guo, J. Liang, Q. Yang, G. Xu, J. Deng, The effects of modified carbon nanotubes on the thermal properties of erythritol as phase change materials, *Energy Convers. Manag.* 157 (2018) 41–48, <https://doi.org/10.1016/j.enconman.2017.11.072>.
- [14] L. Ren, X. Zeng, R. Sun, J.-B. Xu, C.-P. Wong, Spray-assisted assembled spherical boron nitride as fillers for polymers with enhanced thermal conductivity, *Chem. Eng. J.* 370 (2019) 166–175, <https://doi.org/10.1016/j.cej.2019.03.217>.
- [15] H. Malekpour, K.H. Chang, J.C. Chen, C.Y. Lu, D.L. Nika, K.S. Novoselov, A. A. Balandin, Thermal conductivity of graphene laminate, *Nano Lett.* 14 (9) (2014) 5155–5161, <https://doi.org/10.1021/nl501996v>.
- [16] J.D. Renteria, S. Ramirez, H. Malekpour, B. Alonso, A. Centeno, A. Zurutuza, A. I. Cocemasov, D.L. Nika, A.A. Balandin, Strongly anisotropic thermal conductivity of free-standing reduced graphene oxide films annealed at high temperature, *Adv. Funct. Mater.* 25 (29) (2015) 4664–4672, <https://doi.org/10.1002/adfm.201501429>.
- [17] H. Zhou, L. Lv, Y. Zhang, M. Ji, K. Cen, Preparation and characterization of a shape-stable xylitol/expanded graphite composite phase change material for thermal energy storage, *Sol. Energy Mater. Sol. Cells* 230 (2021), <https://doi.org/10.1016/j.solmat.2021.111244>.
- [18] P. Cheng, X. Chen, H. Gao, X. Zhang, Z. Tang, A. Li, G. Wang, Different dimensional nanoadditives for thermal conductivity enhancement of phase change materials: fundamentals and applications, *Nano Energy* 85 (2021), 105948, <https://doi.org/10.1016/j.nanoen.2021.105948>.
- [19] Z.A. Qureshi, H.M. Ali, S. Khushnood, Recent advances on thermal conductivity enhancement of phase change materials for energy storage system: a review, *Int. J. Heat Mass Tran.* 127 (2018) 838–856, <https://doi.org/10.1016/j.ijheatmasstransfer.2018.08.049>.

- [20] J. Duan, Y. Xiong, D. Yang, Study on the effect of multiple spiral fins for improved phase change process, *Appl. Therm. Eng.* 169 (2020), <https://doi.org/10.1016/j.applthermaleng.2020.114966>.
- [21] S. Liu, H. Peng, Z. Hu, X. Ling, J. Huang, Solidification performance of a latent heat storage unit with innovative longitudinal triangular fins, *Int. J. Heat Mass Tran.* 138 (2019) 667–676, <https://doi.org/10.1016/j.ijheatmasstransfer.2019.04.121>.
- [22] M.M. Farid, A. Kanzawa, Thermal performance of a heat storage module using PCM's with different melting temperatures: mathematical modeling, *J. Sol. Energy Eng.* 111 (2) (1989) 152–157, <https://doi.org/10.1115/1.3268301>.
- [23] O.S. Elsanusi, E.C. Nsofor, Melting of multiple PCMs with different arrangements inside a heat exchanger for energy storage, *Appl. Therm. Eng.* 185 (2021), 116046, <https://doi.org/10.1016/j.applthermaleng.2020.116046>.
- [24] L. Kalapala, J.K. Devanuri, Influence of operational and design parameters on the performance of a PCM based heat exchanger for thermal energy storage – a review, *J. Storage Mater.* 20 (2018) 497–519, <https://doi.org/10.1016/j.est.2018.10.024>.
- [25] N. Hu, Z.-R. Li, Z.-W. Xu, L.-W. Fan, Rapid charging for latent heat thermal energy storage: a state-of-the-art review of close-contact melting, *Renew. Sustain. Energy Rev.* 155 (2022), 111918, <https://doi.org/10.1016/j.rser.2021.111918>.
- [26] A. Sciacovelli, F. Gagliardi, V. Verda, Maximization of performance of a PCM latent heat storage system with innovative fins, *Appl. Energy* 137 (2015) 707–715, <https://doi.org/10.1016/j.apenergy.2014.07.015>.
- [27] C. Zhao, M. Opolot, M. Liu, J. Wang, F. Bruno, S. Mancin, K. Hooman, Review of analytical studies of melting rate enhancement with fin and/or foam inserts, *Appl. Therm. Eng.* 207 (2022), 118154, <https://doi.org/10.1016/j.applthermaleng.2022.118154>.
- [28] W. Lin, Z. Ling, Z. Zhang, X. Fang, Experimental and numerical investigation of sebacic acid/expanded graphite composite phase change material in a double-spiral coiled heat exchanger, *J. Storage Mater.* 32 (2020), <https://doi.org/10.1016/j.est.2020.101849>.
- [29] J. Wu, Y. Feng, C. Liu, H. Li, Heat transfer characteristics of an expanded graphite/paraffin PCM-heat exchanger used in an instantaneous heat pump water heater, *Appl. Therm. Eng.* 142 (2018) 644–655, <https://doi.org/10.1016/j.applthermaleng.2018.06.087>.
- [30] W. Lin, W. Zhang, Z. Ling, X. Fang, Z. Zhang, Experimental study of the thermal performance of a novel plate type heat exchanger with phase change material, *Appl. Therm. Eng.* 178 (2020), <https://doi.org/10.1016/j.applthermaleng.2020.115630>.
- [31] M. Medrano, M.O. Yilmaz, M. Nogués, I. Martorell, J. Roca, L.F. Cabeza, Experimental evaluation of commercial heat exchangers for use as PCM thermal storage systems, *Appl. Energy* 86 (10) (2009) 2047–2055, <https://doi.org/10.1016/j.apenergy.2009.01.014>.
- [32] G. Besagni, L. Croci, Experimental study of a pilot-scale fin-and-tube phase change material storage, *Appl. Therm. Eng.* 160 (2019), 114089, <https://doi.org/10.1016/j.applthermaleng.2019.114089>.
- [33] A. Gil, C. Barreneche, P. Moreno, C. Solé, A. Inés Fernández, L.F. Cabeza, Thermal behaviour of d-mannitol when used as PCM: comparison of results obtained by DSC and in a thermal energy storage unit at pilot plant scale, *Appl. Energy* 111 (2013) 1107–1113, <https://doi.org/10.1016/j.apenergy.2013.04.081>.
- [34] G. Peiró, J. Gasia, L. Miró, L.F. Cabeza, Experimental evaluation at pilot plant scale of multiple PCMs (cascaded) vs. single PCM configuration for thermal energy storage, *Renew. Energy* 83 (2015) 729–736, <https://doi.org/10.1016/j.renene.2015.05.029>.